




Cathodic protection mechanism of iron and steel in porous media

Journal Article

Author(s):

[Martinelli-Orlando, Federico](#) ; [Mundra, Shishir](#) ; [Angst, Ueli](#) 

Publication date:

2024-02-16

Permanent link:

<https://doi.org/10.3929/ethz-b-000661995>

Rights / license:

[Creative Commons Attribution 4.0 International](#)

Originally published in:

Communications Materials 5(1), <https://doi.org/10.1038/s43246-024-00454-y>

Funding acknowledgement:

848794 - Towards mastering the long-standing challenge of ageing infrastructures in corrosive environments (EC)

194812 - Enhanced Durability Predictions of Reinforced Concrete Exposed to Corrosive Environments (follow-up proposal) (SNF)

<https://doi.org/10.1038/s43246-024-00454-y>

Cathodic protection mechanism of iron and steel in porous media

Check for updates

Federico Martinelli-Orlando ¹, Shishir Mundra ¹ & Ueli M. Angst ¹ ✉

Cathodic protection was introduced two centuries ago and since has found widespread application in protecting structures such as pipelines, offshore installations, and bridges from corrosion. Despite its extensive use, the fundamental working mechanism of cathodic protection remains debated, particularly for metals in porous media such as soil. Here, we use in-situ and ex-situ characterisation techniques coupled with electrochemical measurements to characterise the spatio-temporal changes occurring at the steel-electrolyte interface. We show that upon cathodic protection, the interfacial electrolyte undergoes alkalisation and deoxygenation, and that depending on polarisation conditions, an iron oxide film can simultaneously form on the steel surface. We further demonstrate that these changes in interfacial electrolyte chemistry and steel surface state result in altered anodic and cathodic reactions and their kinetics. We propose a mechanism of cathodic protection that integrates previous theories, based on both concentration and activation polarisation, complementarily. We discuss the implications of this study in enhancing corrosion protection technologies and the safe, economical, and environmentally friendly operation of critical steel-based infrastructures.

Exactly 200 years ago, Sir Humphry Davy, serving as President of the Royal Society at that time, implemented cathodic protection (CP) as a method to combat metal corrosion for first time on the basis of scientific principles^{1–3}. Capitalising on the late 18th century findings of Galvani and Volta, Davy's experiments showed that coupling sacrificial anodes consisting of relatively unobtainable metals with a more noble metal can protect the latter from corrosion. These findings rapidly led to the large-scale application of CP technology to protect corrosion of copper sheetings of ship hulls of the Royal Navy. While the corrosion of copper in seawater could be effectively mitigated, the protection current caused side effects that greatly impeded the practicality of utilising the technology on ships. Nowadays, it is well understood that these side effects are related to the changes in interfacial seawater chemistry, including an increase in the pH, resulting from the electrochemical reactions occurring on the protected metal surface, and ultimately enabling the formation of mineral deposits and thus promoting fouling^{2,4}. In the early 19th century, Davy was not able to explain these side effects² and failed to resolve them, with serious consequences for the fleet of the Royal Navy and even the relationship between science and society as a whole^{2,3}. Today, the formation of mineral scales upon cathodic protection is widely accepted, and a range of studies have shed light on the parameters controlling the deposition of mineral scales and their properties, especially for cathodically protected steel in seawater. These parameters include

temperature, seawater chemistry (Mg/Ca ratio, pH, etc.), water flow rate, and the extent of cathodic polarisation^{5–7}.

In the early 20th century, CP was increasingly applied to protect steel structures in soil. By now, CP of ground-buried steel structures such as pipes and tank bottoms is among the most widely used corrosion protection technologies^{8–13}, and even required by law in various countries for certain safety-relevant infrastructure such as high-pressure gas lines. In soil, similar electrochemical reactions and changes in electrolyte chemistry as in seawater are expected to occur, although a major difference is that calcareous deposits in soil cannot always form, especially in soft water environments¹¹. Despite the widespread adoption of CP in engineering practices and the long history of CP, fundamental questions about the underlying working mechanism are still under debate^{10–12,14–18}. Divergent theories revolve around two main aspects: the sole consideration of corrosion kinetics^{17,19} on the one hand, and the hypotheses surrounding the formation of iron oxide films on the steel due to the aforementioned changes in electrolyte chemistry^{18,20–31}, on the other hand. On both sides, scholars have mainly argued on the basis of theoretical reasoning and indirect measurements, while thorough investigations about changes in the surface state of the steel electrode (formation of oxide film or not) and the adjacent medium under CP are lacking.

This lack of fundamental and coherent understanding presents a challenge for devising scientifically sound engineering practices, namely

¹Institute for Building Materials (IfB), ETH Zurich, Laura-Hezner Weg 7, CH-8093 Zurich, Switzerland. ✉ e-mail: uangst@ethz.ch

technical guidelines and standards, which are central for the safe, economic, and environmental-friendly operation of various critical steel-based structures, such as in the energy and construction sector. This problem becomes a particularly pressing issue due to the enormous socio-economic importance of corrosion of infrastructure³². In the context of ageing infrastructure in industrialised countries^{33,34}, knowledge-based engineering practices are needed to ensure safety and to mitigate the ever-increasing costs of repairing and replacing deteriorating infrastructures. Moreover, CP can play an important role in reducing the environmental impact of infrastructure globally^{8,35,36}, notably by preventing losses of gas, oil, or water from pipelines and by extending the lifespan of structures.

While CP of steel in flowing electrolytes such as seawater is largely understood, CP of steel in porous media such as soil or concrete, is comparatively poorly understood, because of additional degrees of complexity stemming from aspects such as the tortuous nature of the system – limiting mass transport processes such as ion or oxygen diffusion and advection, or because of the variability in the electrolyte chemistry encountered in these porous media. For these reasons, this work aimed at unravelling the mechanism of CP of steel in a porous media, such as that of soil. Here, we use a comprehensive approach utilising in-situ and ex-situ spectroscopic and microscopic techniques, combined with electrochemical characterisation, to study the changes at the metal-electrolyte interface, and particularly at the metal surface, during cathodic polarisation.

Results

Time-resolved in-situ characterisation

We potentiostatically polarised carbon steel specimens immersed in electrolyte to different cathodic or ON-potentials (E_{ON}) and recorded the cathodic current density (or protection current density, i_{prot}). This current density i_{prot} was found to drastically increase with more negative E_{ON} (Fig. 1a). It is noticeable that in the simulated soil solution, i_{prot} decreased over time, which indicates time-dependent changes in electrolyte chemistry or electrode reaction kinetics. Within ~ 10 h, however, i_{prot} tended to

stabilise, reaching steady-state values of $\sim 4 \text{ A m}^{-2}$ (at -1.2 V_{SSE}), $\sim 0.4 \text{ A m}^{-2}$ (at -1.0 V_{SSE}), $\sim 0.25 \text{ A m}^{-2}$ (at -0.9 V_{SSE}), and $\sim 0.1 \text{ A m}^{-2}$ (at -0.8 V_{SSE}).

The application of i_{prot} enhances the cathodic reactions occurring at the steel surface, in particular the oxygen reduction reaction (ORR) and the hydrogen evolution reaction (HER). According to these reactions, the local pH at the metal-solution interface is expected to increase. We quantified this increase in pH in simulated soil solutions in a separate experimental setup. Small and minimally invasive pH sensors were installed at a given distance from the carbon steel electrode to monitor the time-dependent pH changes in simulated soil solution upon polarisation. Figure 1b shows that the pH in the electrolyte in vicinity of the metal surface increased. At a distance of 6 mm from the polarised steel, the pH of the simulated soil solutions ranged between pH 8–10 (at -0.92 V_{SSE}) and pH 10–13 (at -1.10 V_{SSE}) within a few hours of polarisation. The pH profiles shown in Fig. 1c suggest even higher pH values at the steel surface. These observations of alkalisation are qualitatively in agreement with literature^{16,22–25,37,38}. To further corroborate the electrochemistry-driven alterations in near-surface electrolyte chemistry, the concentration of dissolved oxygen was measured with small sensors positioned at distance 6 mm from the steel surface in the same setup where pH measurements were done. Figure 1d shows that oxygen is rapidly consumed upon application of i_{prot} , supporting the aforementioned hypothesis that oxygen reduction reaction (ORR) occurs, and then, once the dissolved oxygen concentration has decreased to very low levels, the hydrogen evolution reaction (HER) may dominate.

For comparison with the initially pH near-neutral simulated soil solution, we exposed carbon steel directly ($t = 0$) to an alkaline solution with pH ~ 13 and potentiostatically polarised to $E_{ON} = -0.8 \text{ V}_{SSE}$. In this case, i_{prot} showed less pronounced changes over time, apart from a relatively small decrease within the first hour, and stabilised at a value of $\sim 0.2 \text{ A m}^{-2}$ (Fig. 1a). Since the electrolyte used had an elevated concentration of OH^- ($\sim 0.1 \text{ M}$), the application of the cathodic current in the order of 0.25 A m^{-2} is not expected to increase the pH significantly in the vicinity of the sample.

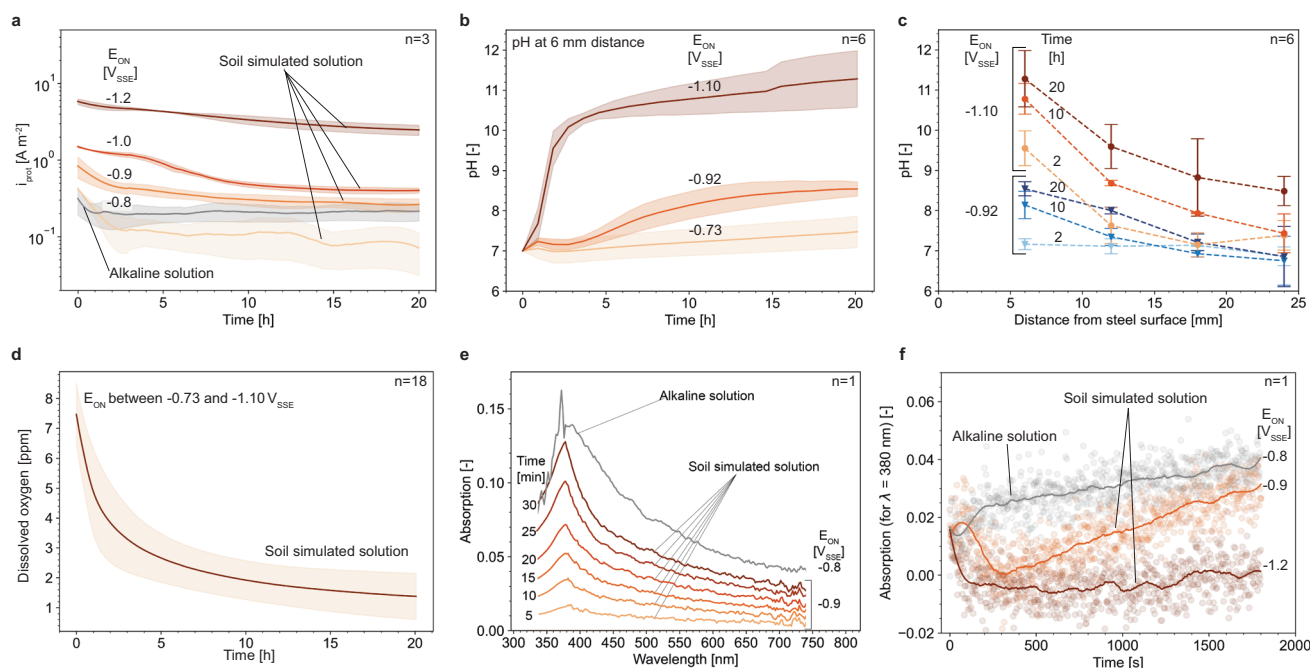


Fig. 1 | Time-resolved in-situ characterization of the steel / porous medium interface. **a** Mean (line) and standard deviation (shade) of the protection current densities applied for the different E_{ON} and electrolytes. **b** Mean (line) and standard deviation (shade) of the in-situ pH measurements at 6 mm distance from the WE surface as a function of the applied E_{ON} and experimental time. **c** Mean and standard deviation of the pH measured upon CP as a function of the distance from the WE surface, experimental time, and E_{ON} . **d** Mean (line) and standard deviation (shade)

of the dissolved oxygen (DO) concentration as a function of the experimental time for E_{ON} between -0.73 and -1.1 V_{SSE} measured at 6 mm from the surface of the WE. **e** Light absorption spectra over time for the samples polarised to -0.8 V_{SSE} and -0.9 V_{SSE} in alkaline and soil simulated solution, respectively. **f** Absorption of the light with wavelength 380 nm for samples under polarisation in alkaline and soil simulated solution. The number of samples (n) used for the statistical analysis is indicated in each figure.

It is interesting that i_{prot} reached a comparable value in alkaline (pH~13) solution after ~1 h and in initially pH near-neutral simulated soil solution after ~10 h.

According to well-established theory³⁹, under alkaline conditions and with potentials more noble than the reversible potential of the Fe/Fe(II) electrode, the formation of an iron oxide film is expected. We tested this hypothesis of oxide film formation upon cathodic polarisation by measuring in-situ the absorption on the surface of carbon steel samples for a duration of 30 min, using UV-Vis spectroscopy. In simulated soil solution of initial near-neutral pH and polarised at $E_{ON} = -0.9 V_{SSE}$, the absorption spectra (Fig. 1e) increased over the experimental time, particularly in the UV region (wavelengths (λ) <400 nm, also in line with observations in the literature³⁴⁻³⁶) and with a characteristic peak at $\lambda = 380$ nm. Similarly, in alkaline solution (pH ~ 13) polarised at $E_{ON} = -0.8 V_{SSE}$ (Fig. 1e), the absorption on the steel surface showed a peak at $\lambda = 380$ nm. This suggests comparable surface states for steel cathodically polarised in an initially alkaline electrolyte, and cathodically polarised steel in an initially pH near-neutral electrolyte (that transformed to an alkaline electrolyte upon polarisation at $E_{ON} = -0.9 V_{SSE}$).

Additionally, we monitored the film formed on the steel surface over time, by conducting in-situ photometric reflectance measurements (PRM) at $\lambda = 380$ nm. At $E_{ON} = -0.9 V_{SSE}$ in simulated soil solution, the absorption of the film was found to increase during the entire course of the experiment (Fig. 1d), indicative of film growth. When the steel was exposed to an already initially highly alkaline electrolyte, the adsorption increased more rapidly than in the initially pH near-neutral simulated soil solution at $E_{ON} = -0.9 V_{SSE}$; however, after 30 min comparable adsorption (suggesting comparable film thickness) was observed. In the case of polarisation at $E_{ON} = -1.2 V_{SSE}$ in simulated soil solution, the formation of an oxide film was not evident over the entire course of the experiment. This may be expected from the Pourbaix diagram (Supplementary Fig. 5) for iron that reveals that such negative polarisation lies within the immunity domain⁴⁰.

Given the similarity in the i_{prot} and absorption data from UV-Vis spectroscopy and PRM for steel immersed in an already initially alkaline (pH ~ 13) solution, polarised at $E_{ON} = -0.8 V_{SSE}$, and steel immersed in simulated soil solution (initial pH 7.3), polarised at $E_{ON} = -0.9 V_{SSE}$, we would be reasonable in expecting the iron oxide film formed on the samples exposed to the two electrolytes being similar in composition and thickness for the considered experimental time and conditions.

Ex-situ surface characterisation

While in-situ methods allow us to identify the presence or absence of a supposed iron oxide film and monitor its growth over time, ex-situ methods allow obtaining quantitative information and mapping the chemical composition of the interface of interest upon termination of the experiments. FIB-TEM, STEM and EDS was conducted on carbon steel, ex-situ, after 20 h of polarisation in either simulated soil solution or alkaline solution at different E_{ON} . The efficacy of our sample preparation protocol was tested by viewing a freshly polished steel sample under the TEM (Supplementary Fig. 1) and was validated by the absence of an oxide film at the interface between the freshly polished steel surface and the Pd/Pt coating. The TEM/STEM/EDS micrographs (Fig. 2 and Supplementary Fig. 1) show the presence of an oxide film (rich in Fe and O from the EDS maps) on the steel surface after polarisation to potentials $-0.8 V_{SSE}$, $-0.9 V_{SSE}$, and $-1.0 V_{SSE}$ in simulated soil solution, and $-0.8 V_{SSE}$ in the highly alkaline electrolyte. For all these cases, an oxide film with a thickness of ~2–5 nm was observed. As would be expected for the case of polarising the steel at $-1.2 V_{SSE}$, in the immunity region of the Pourbaix diagram⁴⁰ as mentioned above, an oxide film could not be observed. Note that this is also in line with the almost constant zero absorption at $\lambda = 380$ nm over time in the PRM measurements (Fig. 1f). These ex-situ micrographs confirm that the peak in the absorption spectra at $\lambda = 380$ nm (observations from in-situ UV-Vis spectroscopy (Fig. 1e)) is related to the presence of an iron oxide film.

Electrochemical impedance spectroscopy

We assessed the electrochemical properties of the metal-solution interface over time, when immersed in simulated soil solution and maintained at different E_{ON} , using electrochemical impedance spectroscopy (EIS). In general, the EIS measurements varied significantly depending on the E_{ON} and over experimentation time. For all E_{ON} , an increase in the real and imaginary parts of impedance can be observed from the Nyquist plots (Fig. 3) over time. From the Lissajous plots acquired at 0.01 Hz (Fig. 3a) which is a frequency associated with negligible capacitive effects (see Supplementary Fig. 2), we could observe the current density to shift to lower values over time. This is in agreement with the i_{prot} in Fig. 1a.

At $E_{ON} = -0.8 V_{SSE}$, we found that the currents during the sinusoidal applied voltage signal included both cathodic and anodic excursions (Fig. 3a), suggesting that the system was close to the open circuit potential (OCP) over the entire experimental time, as one would expect in deoxygenated conditions. This can be explained by the known rapid deoxygenation of the metal surface upon application of a cathodic protection current^{23,24} (Fig. 1d), which is also supported by the observed fast decrease in i_{prot} below levels of $0.1 A m^{-2}$ (Fig. 1a). Given that this system was close to the OCP, we estimated the polarisation resistance (Supplementary Note 1) from the slope of the Lissajous plots (acquired at 0.01 Hz, Fig. 3a). Conversion to corrosion current density suggests the latter to be of the order of $\sim 7 \mu A cm^{-2}$ (or $\sim 70 \mu m y^{-1}$, Supplementary Note 1), which is clearly higher than protection criteria in different standards^{41,42}. It can therefore be inferred that at $E_{ON} = -0.8 V_{SSE}$ cathodic protection was not fully achieved and the metal corroded at non-negligible values, however at a much lower rate than a non polarised steel exposed to a similar electrolyte⁴³. We observed remarkably different electrochemical impedance spectra for the cases at $E_{ON} = -0.9 V_{SSE}$ and $E_{ON} = -1.0 V_{SSE}$ and these show a significant increase in impedance over time, with real impedances reaching $>4000 \Omega cm^2$ after 20 h. At $E_{ON} = -0.9 V_{SSE}$, there seems to be a second time constant at low frequencies appearing with time, although the data generally becomes relatively noisy after 5–10 h, which hampers the interpretation at frequencies <0.1 Hz. For the case at $E_{ON} = -1.2 V_{SSE}$, the Nyquist plots (Fig. 3e) showed perfect semicircles, especially after 10 h of polarisation, suggestive of an ideal capacitive metal/solution interface. In line with the observations from PRM (Fig. 1f) and FIB-TEM (Fig. 2), at $E_{ON} = -1.2 V_{SSE}$, the carbon steel was virtually free of an oxide film. For all other polarisation conditions ($E_{ON} = -0.8 V_{SSE}$, $E_{ON} = -0.9 V_{SSE}$ and $E_{ON} = -1.0 V_{SSE}$), the semicircles were depressed (Fig. 3b–d) and indicative of a corroding or passive iron system⁴⁴, which again agrees with the in-situ and ex-situ surface characterisation results presented above. It may also be noted that at $E_{ON} = -1.2 V_{SSE}$, while the impedance increased over time, it was much lower ($800 \Omega cm^2$ at 20 h) compared to all other studied polarisation conditions, which may be attributed to the fast kinetics of the HER, as discussed below.

Conducting EIS in conjunction with polarising the carbon steel at significantly cathodic potentials ($E_{ON} = -1.0 V_{SSE}$ and $-1.2 V_{SSE}$) allowed us to extract interesting information from the Lissajous plots at frequency 0.01 Hz, where capacitive effects can here be considered negligible. At these cathodic potentials, the potential-current response of the system can be assumed to be governed by the kinetics of the cathodic reaction and the Lissajous plots can be considered to represent a small portion of the cathodic reaction branch. For instance, the slope of the Lissajous plots can be used as a proxy of the cathodic Tafel slope (b_c , Supplementary Note 1). Given that the concentration of dissolved oxygen at the steel surface decreases rapidly to low values (Fig. 1d), it is reasonable to assume that this cathodic Tafel slope over time corresponds increasingly to the cathodic reaction kinetics of the HER. At $E_{ON} = -1.0 V_{SSE}$, $|b_c|$ increased with time, approaching a value of $0.45 V dec^{-1}$ (Supplementary Note 1), which is in line with literature values for HER on carbon steel with an iron oxide film⁴⁵. The change in b_c over time suggests increasingly limited HER kinetics, which agrees with our results on time-dependent i_{prot} , pH, dissolved oxygen, PRM (Fig. 1) and the FIB-TEM (Fig. 2) confirming the presence of an iron oxide film. On the other hand, at $E_{ON} = -1.2 V_{SSE}$, the opposite trend for $|b_c|$ was observed, namely a

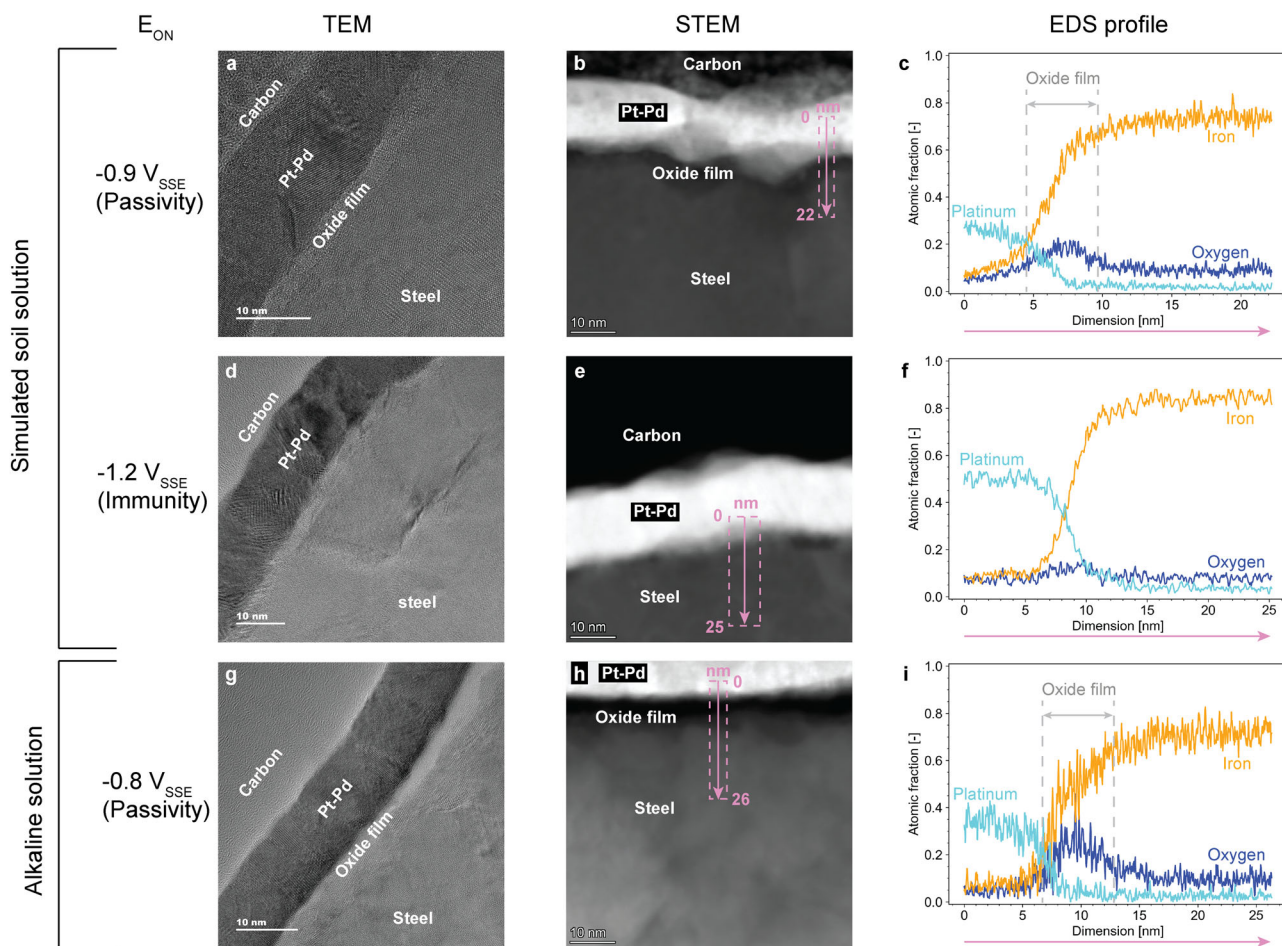


Fig. 2 | Ex-situ characterisation of steel surfaces. Ex-situ TEM micrographs (a, d, g), high-angle annular dark-field STEM micrographs (b, e, h) and EDS profiles of iron, oxygen, and platinum (c, f, i). The location and direction of the EDS profiles is indicated on the STEM-EDS maps by means of purple arrows; the dashed box indicates the averaged width. The data was obtained for samples polarised for 20 h to $E_{ON} = -0.9 V_{SSE}$ (a–c) and $E_{ON} = -1.2 V_{SSE}$ (d,e,f) in simulated soil solution as well as $E_{ON} = -0.8 V_{SSE}$ in alkaline solution (g, h, i).

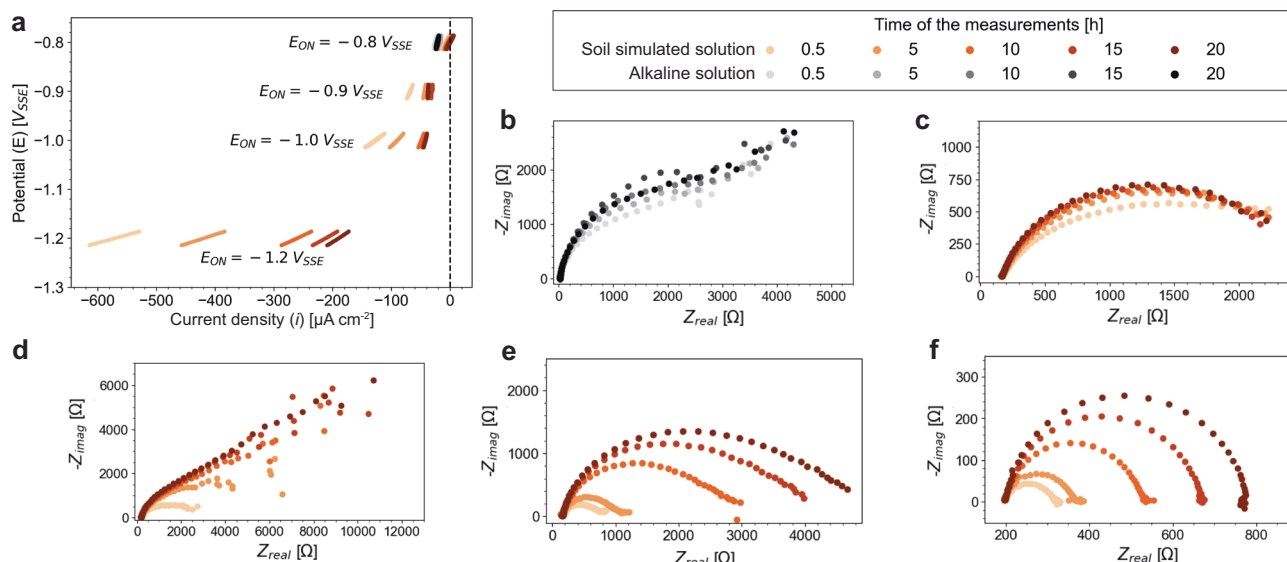


Fig. 3 | In-situ characterisation by means of electrochemical impedance spectroscopy. a Lissajous plots acquired for 0.01 Hz at different E_{ON} as a function of the experimental time. Nyquist plots measured on carbon steel under cathodic polarisation as a function of the experimental time for (b) $E_{ON} = -0.8 V_{SSE}$ in alkaline solution, and (c) $E_{ON} = -0.8 V_{SSE}$, (d) $E_{ON} = -0.9 V_{SSE}$, (e) $E_{ON} = -1.0 V_{SSE}$, (f) $E_{ON} = -1.2 V_{SSE}$ in soil simulated solution.

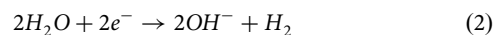
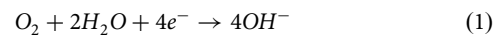
decrease in $|b_c|$ towards values around 0.3 V dec^{-1} (Supplementary Note 1). This may be explained by the fact that the $|b_c|$ of HER is lower on bare iron compared to iron covered with an oxide film⁴⁵, and that at $E_{\text{ON}} = -1.2 \text{ V}_{\text{SSE}}$, the steel electrode is in the immunity domain and is free from an oxide film (Fig. 2).

Discussion

Based on our investigations of both spatio-temporal changes in the electrolyte and of the steel surface, we provide a closure to the long-standing debate on the working principle of CP. A century after Davy's experiments to protect copper in seawater from corrosion, CP of iron and mild steel in soil – a porous medium – was studied by Bauer and Vogel in Germany in the 1910s⁴⁶ and extensively by Kuhn in the US in the 1920s⁴⁰. From the 1950s onwards, CP was also applied to protect reinforcing steel corrosion in another porous medium, namely concrete⁴⁷. CP of iron-based alloys exhibits fundamental differences from CP of copper, amongst other reasons, because iron in the water system cannot be as easily polarised to the immunity domain as in the case of copper³⁹. While the work by Bauer and Vogel⁴⁶ was largely inspired by Davy's approach and focused on varying the area ratio between sacrificial anodes such as zinc and the protected iron, Kuhn⁴⁰ carried out more rigorous experiments, striving to elucidate the underlying mechanism. Already in 1928, Kuhn hypothesised – notably without any direct experimental evidence – on the role of changes in the interfacial electrolyte chemistry by stating that the cathodic current “causes a film of hydroxide to form which protects these areas from corrosion” (in agreement with Eqs. 1 and 2, shown below). Later on, scholars^{9,21–25,29,30,38,48–51} have attempted to experimentally quantify this modification of the electrolyte upon CP, which was later interpreted in the context of pH-dependent stability diagrams that were proposed by Pourbaix in the middle of the last century³⁹. This combination of experimental evidence for interfacial pH increases upon CP with thermodynamic stability diagrams, made a number of scholars hypothesise about the formation of an iron oxide film that then protects the steel from corrosion^{11,25,28,31,37,38,52–58}. Note that in the literature, and especially in the work of Pourbaix, such films forming within the potential-pH domain where iron oxides are thermodynamically stable, are termed passive film, because the film significantly modifies the anodic reaction kinetics, namely slowing down the iron dissolution rate by several orders of magnitude, thus promoting corrosion protection. However, direct experimental evidence for such oxide films was lacking until today. Another camp of scholars remained critical about a oxide film forming under cathodic polarisation and instead supports the view that the mechanism of CP of steel occurs through the negative shift in potential along the Tafel line of the activation-controlled iron dissolution reaction ($\text{Fe} \rightarrow \text{Fe}^{2+} + 2e^-$), thus reducing the rate of anodic iron dissolution^{13,17,19}.

We conclude that both these theories need to be considered complementary to each other, rather than contradictarily, to fully elucidate the working mechanism of CP as highlighted in Fig. 4a–c and discussed in the following. Prior to application of a cathodic current, at $t < 0$ (Fig. 4a), the anodic dissolution of Fe is sustained by the oxygen reduction reaction (ORR, Eq. 1), generally under diffusion limited conditions. The released aqueous Fe hydrolyses and precipitates as Fe(II) oxides or, upon oxidation, as Fe(III) (hydr)oxides. As shown in Fig. 4b, in the early stage of the application of a cathodic current, at $t \geq 0$, our results indicate that the pH of the electrolyte in the vicinity of the steel increases (Fig. 1b, c) and that this local alkalisation of the electrolyte is accompanied by a reduction in dissolved oxygen (Fig. 1d). These changes in the interfacial electrolyte chemistry (e.g., rise in pH and reduction in the dissolved oxygen concentration) may also explain the increase of the phase angle over the experimental time in the frequency region between 1000 and 1 Hz obtained with EIS measurements (Supplementary Fig. 2). Equation 1 shows the simultaneous consumption of oxygen and generation of OH⁻, occurring for ORR, and leading to a decrease of oxygen concentration and an increase of pH at the metal surface, which over time, due to diffusional transport, leads to concentration profiles (the magnitude of which might be influenced by the degree of saturation) extending into the porous medium as schematically illustrated in Fig. 4b and

apparent from the experimental results (Fig. 1b, c). With time and decreasing concentration of dissolved oxygen (Fig. 1d), the ORR is overtaken by the hydrogen evolution reaction (HER) as the cathodic reaction, further resulting in the generation of OH⁻ (Eq. 2).



A rise in the local pH (Fig. 1b, c), modifies the thermodynamic stability of the polarised steel-electrolyte interface (as viewed through the Pourbaix diagram for Fe-H₂O – Supplementary Fig. 5) from the active domain to the passive domain, facilitating the growth of an iron oxide film with composition predominantly resembling that of magnetite (Fe₃O₄)³⁹ (Fig. 4c). The formation of such an oxide film has been experimentally shown both with in-situ (Fig. 1e, f) and ex-situ (Fig. 2, Supplementary Fig. 1) measurements, and quantified at a thickness of ~2–5 nm. Our time-resolved in-situ measurements (Fig. 1e, f) suggest that the oxide film grows as the pH at the metal-electrolyte interface increases over time (Fig. 1b, c). The fact that the measured absorption increases (Fig. 1f) significantly faster for steel when cathodically polarised in an initially ($t = 0$) already alkaline solution than in the case when the steel is cathodically polarised in an initially near-neutral solution (and consequentially leading to an alkaline solution at the steel-electrolyte interface), further corroborates our hypothesis that the formation of an iron oxide film is a direct consequence of the increase in pH.

The application of cathodic polarisation not only changes the electrolyte chemistry and the surface state of the steel, but also simultaneously influences the corrosion kinetics, as indicated by the marked decrease in the i_{prot} observed over time (Fig. 1a). We explain this decrease in i_{prot} with a schematic Evans diagram – as illustrated in Fig. 4d, e. Let us first understand how CP influences the cathodic reaction kinetics. Upon the application of a cathodic current ($t \geq 0$), the electrolyte at the steel-electrolyte interface becomes alkaline and depleted in dissolved oxygen within a few hours (Fig. 1), and, as a consequence as discussed above, the dominating cathodic reaction changes from ORR to HER. In systems with low bulk oxygen concentration, e.g. in wet soil, this transition will obviously occur faster. In any case, the local alkalisation of the electrolyte due to ORR and HER at the steel-electrolyte interface modifies the reversible potential of hydrogen ($E_{\text{H}_2}^{\text{rev}}$) to more negative values³⁹. The cathodic Tafel slopes obtained from the Lissajous plots, and especially their evolution over time (Fig. 3a and Supplementary Note 1), support the suggested changes in the cathodic reaction, from ORR to HER, and the growth of an oxide film on the metal surface with time (Fig. 4c, d).

Now, we consider the changes in the anodic reaction kinetics upon cathodic polarisation. The oxide film formed due to the alkaline pH (>9) at the steel-electrolyte leads to a drastic change in the anodic reaction kinetics, as evidenced by the conversion of the anodic reaction from iron dissolution ($\text{Fe} \rightarrow \text{Fe}^{2+} + 2e^-$) to magnetite formation ($3\text{Fe} + 4\text{H}_2\text{O} \rightarrow \text{Fe}_3\text{O}_4 + 8e^- + 8\text{H}^+$)⁵⁹. With this transition, the reversible potential of the anodic reaction ($E_{\text{Fe}}^{\text{rev}}$) becomes pH dependent³⁹, and the Tafel slope increases significantly, reflecting the hindered anodic dissolution kinetics. By considering these dynamic changes in the anodic and cathodic reaction kinetics, the composition (particularly pH) of the electrolyte, the concentration of dissolved oxygen at the steel-electrolyte interface and the surface state of the steel, we can explain the decrease in the i_{prot} over time (Fig. 4d). Our results suggest stabilisation at longer durations between 0.05 A m^{-2} and 4 A m^{-2} (depending on the cathodic potential applied).

However, as one would expect, the growth of the iron oxide film would only be possible when the pH is sufficient high and the potential is above $E_{\text{Fe}}^{\text{rev}}$, for there to be a residual anodic current density (Fig. 4d, e), and not to force the steel-electrolyte interface into the immunity region of the Fe-H₂O Pourbaix diagram (Supplementary Fig. 5). Finally, it should be noted that if one assumed that the anodic and cathodic kinetics are constant (that is, not affected by the changes due to the cathodic polarisation, and remaining as

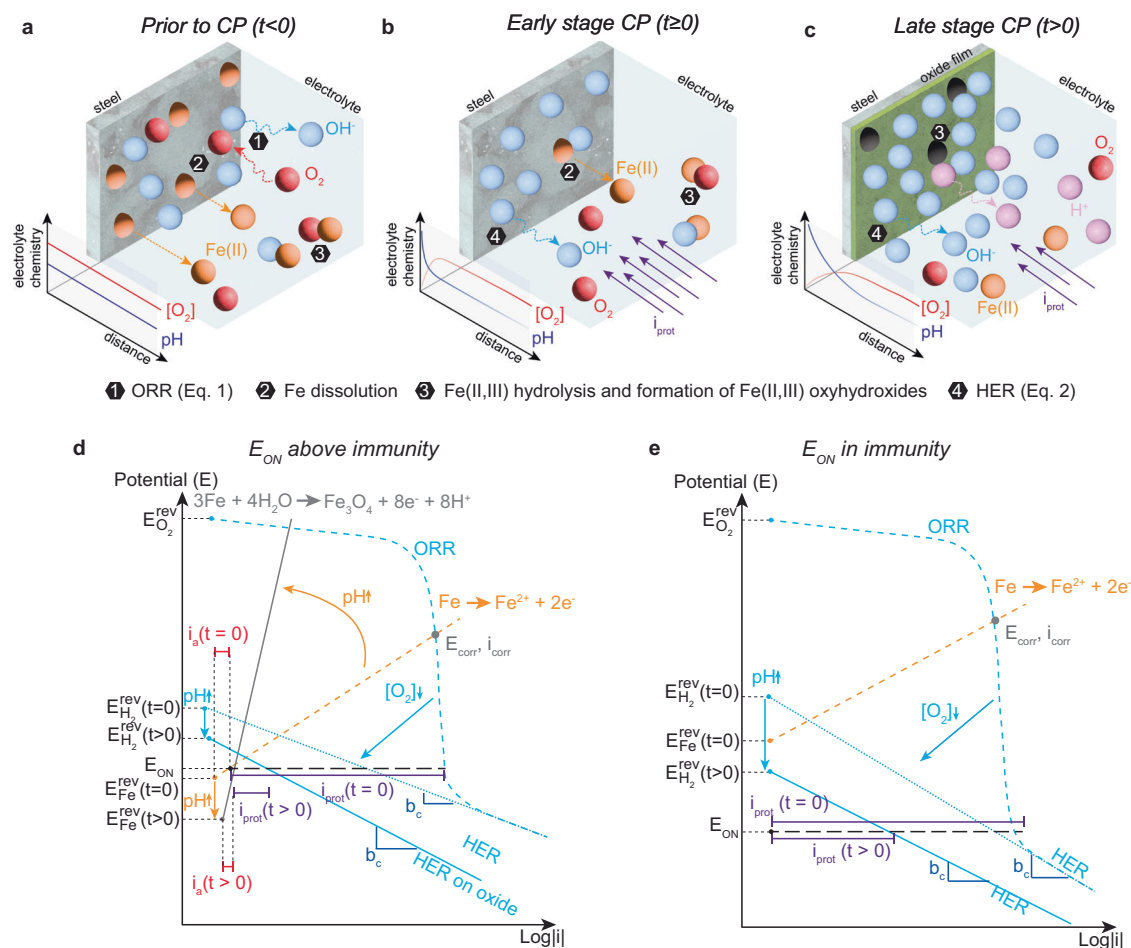


Fig. 4 | Mechanism of cathodic protection of iron or carbon steel. Schematic representation of cathodic protection mechanism (a) before the application of CP, (b) in the first instants of CP application, (c) and later during CP application. Schematic representation of the Evans diagram for iron or carbon steel in passive domain (d) and in immunity (e) in simulated soil solution with an initial pH 7.3. The kinetics reported here refer to the Pourbaix diagram. The blue lines correspond to the cathodic reactions (Eq. 1 and Eq. 2) and the orange lines correspond to the anodic reaction (iron dissolution). Dotted lines represent time (t) equal to 0, namely the

moment of the application of the cathodic current, continuous lines are at $t > 0$, that is, a time where the application of the cathodic current has led to an increase in pH and a decrease in oxygen concentration at the metal surface. The dashed black lines correspond to E_{ON} , the purple line correspond to the applied cathodic current density (i_{prot}), while the red line corresponds to the residual anodic current density (i_a). E_{corr} and i_{corr} correspond to the open circuit potential (OCP) and corrosion current density, respectively, in absence of polarisation. b_c represents the cathodic Tafel slope on bare metal and on iron oxide.

represented for $t = 0$ in Fig. 4d also for $t > 0$, the experimental observations of a decrease in i_{prot} over polarisation time could not be explained.

This study has characterised a number of simultaneous and intertwined processes occurring at the steel-porous medium interface upon the application of CP, namely, alkalisation and deoxygenation of the interfacial electrolyte and the formation of an iron oxide film on the steel surface. Whilst our results coherently underpin the proposed mechanism of CP of steel in porous media summarised in Fig. 4, it is important to note that the thermodynamic stability domains of immunity, active corrosion, and passivity depends on the activity of Fe and the presence of species such as chloride, sulfates, or carbonates. Thus, the here observed relationships between applied potential (E_{ON}), resulting protection current, pH, oxygen concentration, and growth of oxide film, are not directly applicable to other conditions. In particular the effect of complexing species such as carbonate ions may have an important influence on E_{ON} needed to ensure corrosion protection (compare Supplementary Note 2)⁶⁰.

The findings and mechanistic insight of this study contribute to enhancing corrosion protection technologies and resolving some of the severe limitations of the state-of-the-art engineering practices related to corrosion in safety-relevant steel-based structures, such as in the energy and construction sector. Criteria for the assessment of the effectiveness and to ensure the safe operation of CP have been debated for almost a

century^{11,12,18,29,49,61–63}, with the controversy arising primarily from a lack of scientific comprehension of the mechanism of CP. It should also be mentioned that protection criteria in standards are largely based on empiricism rather than on scientifically rigorous concepts^{10,11,49,64}. Interestingly, our findings now support the plausibility and correctness of certain concepts in these standards (Supplementary Note 3). Nevertheless, a severe shortcoming of state-of-the-art engineering is that the requirements specified in various standards sometimes conflict with one another, making it difficult to satisfy all relevant standards simultaneously^{10,64}. To overcome these limitations of engineering practice, new approaches have been proposed⁶⁴. It is important to recognise that these approaches are based on the previously hypothesised concept that an iron oxide film forms upon CP^{10–12,16,20,26}. In this context, our findings serve as a crucial basis for future engineering practice to devise consistent standards that are not in conflict with each other and are based on parameters that can be measured on modern and well-coated structures.

Materials and methods

Materials and experimental setups

Carbon steel (grade 1.0330, with C < 0.12%, Mn < 0.6%, P < 0.045% and S < 0.045%, according to the specifications of the supplier) was used as the working electrode (WE) in this study. The reference electrode (RE) was Ag/

AgCl sat. KCl (SSE) and the counter electrode (CE) was titanium metal mixed oxides (TiMMO) mesh. NaOH pellets ($\geq 98\%$), anhydrous Na_2SO_4 ($>99\%$), NaHCO_3 ($>99.7\%$) and Ethylenediaminetetraacetic acid disodium salt dihydrate (EDTA) ($>99\%$) of ACS reagent grade were purchased from Sigma Aldrich. For all the experimental setups used in this study, stirring of the electrolyte was not implemented.

Setup for steel characterisation. The WE was a cylindrical carbon steel bar with its lateral surface coated with epoxy resin, which was applied with fluidised bed epoxy coating technique. With this process, possible gaps between the steel and the epoxy resin are minimised, thereby, reducing the risk of crevice corrosion. After soldering the back side of the sample to a copper cable to provide electrical connection, the sample was embedded in an acrylic resin, protecting the cable connection at the back side as well as the lateral surface. The uncoated front surface of the bar, which has a cross-sectional area of 1 cm^2 , was polished down to $1\text{ }\mu\text{m}$ with a diamond paste and then exposed to electrolytes for all subsequent tests. Between polishing and immersion in the electrolyte, the sample was stored for 30 min in a desiccator containing silica gel (i.e. relative humidity about 10%).

Two electrolytes were used in this study: an alkaline solution composed of $0.1\text{ M NaOH} + 2\text{ mM EDTA}$ with pH equal to 13, and a simulated soil solution composed of $5\text{ mM Na}_2\text{SO}_4 + 2.5\text{ mM NaHCO}_3 + 2\text{ mM EDTA}$ with pH equal to 7.3. The conductivities of the alkaline solution and simulated soil solution measured with Mettler-Toledo SevenExcellence conductivity electrode were $22310\text{ }\mu\text{S cm}^{-1}$ and $1341\text{ }\mu\text{S cm}^{-1}$, respectively. EDTA is well known to have a strong affinity for aqueous iron^{65,66} and reduce the availability of aqueous iron to participate in other chemical reactions^{65–67}. EDTA was added in the electrolytes to minimise the precipitation of iron hydroxides at the metal surface^{68,69}, which could potentially interfere with in-situ surface characterisation. EDTA is generally not present in natural environments, but other species (i.e., carbonate ions, CO_3^{2-} ^{48,60}) with similar affinity to iron might be present in natural soils.

The pH of the solutions was measured by means of Mettler-Toledo SevenExcellence pH meter in conjunction with a glass membrane electrode. The pH meter was calibrated against commercial (Mettler-Toledo and Sigma-Aldrich) buffer solutions of pH 7, 11 and 13. The measurements in alkaline solutions were performed relatively quickly to reduce the error as a consequence of the release of silica from the glass membrane.

Setup for electrolyte characterisation. In order to limit the setup to a 1D problem, an electrochemical cell with internal dimensions $20 \times 20 \times 200\text{ mm}^3$ was designed to study the temporal and spatial modifications in the soil chemistry during the application of CP (Supplementary Fig. 4).

The dimensions of the WE for this setup were $19 \times 19 \times 2.5\text{ mm}^3$. The back side of the WE was soldered to a copper wire to provide electrical connection. Subsequently the WE was embedded in acrylic resin to isolate the back side as well as the lateral side from the electrolyte. The WE was polished down to $5\text{ }\mu\text{m}$ with SiC grinding paper leaving an exposed area of 3.61 cm^2 . The WE was then located on one of the sides of the electrochemical cell. On the opposite face of the cell, the CE was positioned at a distance of $\sim 195\text{ mm}$ from the surface of the WE. The RE was positioned 6 mm away from the surface of the WE to limit the contribution of IR-drop during the measurements.

Potentiometric sensors (Duramon AG), to measure pH in-situ, were positioned at 6 mm , 12 mm , 18 mm , and 24 mm from the WE surface. Additionally, an optical sensor (Pyroscience GmbH) was placed at 6 mm from the WE surface to monitor dissolved oxygen (DO) concentration. The location of the pH and oxygen sensors allowed monitoring temporal and spatial changes in the chemistry of the electrolyte in proximity of the WE upon the application of CP.

For these experiments the electrolyte was composed by quartz sand with granulometry $<0.9\text{ mm}$ saturated with a solution composed by $5\text{ mM Na}_2\text{SO}_4 + 2.5\text{ mM NaHCO}_3$ and adjusted to a pH of 7 by adding HCl. The

conductivity measured with Mettler-Toledo SevenExcellence conductivity electrode of the soil saturated solution was $437\text{ }\mu\text{S cm}^{-1}$.

Before the experiment, the quartz sand was carefully washed with dionised water and dried in oven at $80\text{ }^\circ\text{C}$ multiple times until the conductivity of the washed out water was in the same range as the conductivity of the dionised water. These iterations were performed to remove possible contaminants that could compromise the chemical composition of the solution.

Electrochemical polarisation and measurements

The electrochemical conditioning and measurements were performed with Gamry interface 1010E. On all samples, cathodic polarisation was applied in potentiostatic mode up to 20 h. Different ON-potentials (E_{ON}) in the range of $-0.73\text{ V}_{\text{SSE}}$ and $-1.20\text{ V}_{\text{SSE}}$ were applied. The corresponding cathodic protection current densities (i_{prot}), were recorded over time. The electrochemical cell used for these electrochemical polarisation tests and measurements combined with PRM and UV-vis spectroscopy is described elsewhere^{48,70}.

Additionally, companion samples were identically polarised in a conventional three-electrode electrochemical cell, which allowed for in-situ characterisation by means of electrochemical impedance spectroscopy (EIS). EIS measurements were repeated once with a fresh sample for each configuration. As the results showed very good reproducibility, data pertaining to only one sample is presented in this paper.

Upon polarising the sample cathodically, EIS was conducted every 30 min for 20 h. To this aim, a sinusoidal voltage signal was superimposed on different E_{ON} . The superimposed root-mean-squared voltage signal (V_{RMS}) was 15 mV . The frequency range used to study EIS was between 5000 Hz and 0.01 Hz .

Steel and electrolyte characterisation techniques

UV-vis (in-situ). UV-vis measurements were carried out using a Lambda 650 UV-Vis spectrophotometer from Perkin Elmer. The absorption spectra were recorded between wavelengths 800 and 320 nm , with step size of 2 nm . The electrochemical cell was located at the reflection station of the UV-vis spectrophotometer, and the WE was positioned in correspondence to the centre of the incident light window (with a diameter about 2.5 cm). The WE surface was positioned 4 mm from the Suprasil glass of the electrochemical cell, making the effective path length of light roughly 8 mm . The reflected and scattered light were collected by the integrating sphere and directed to the detector.

Photometric reflectance measurements (in-situ). For photometric reflectance measurements (PRM), a Deuterium lamp (30 W) was used as the light source, providing a continuous light with wavelength between 200 nm and 700 nm (UV and visible range). An optical fibre with diameter of $400\text{ }\mu\text{m}$ and 2 m in length guided the light towards the WE surface. Ferrule clamps and a 3D printed support in polylactic acid (PLA) allowed positioning the optical fibres at a distance of $6 \pm 0.15\text{ mm}$ from the WE, with an incident (α_i) and reflection angle (α_r) of $30^\circ \pm 0.2^\circ$. The diameter of the light beam on the WE surface was about 2 mm . The reflected light was collected by means of a second optical fibre and guided to the spectrometer (Thorlabs CCS200). The spectrometer and the potentiostat were connected via USB to a computer and controlled with the dedicated software. Schematic representations of the setup can be found in Supplementary Fig. 6 and a detailed description of the setup has been reported elsewhere^{48,70}.

The absorption of the film was calculated with Eq. 3⁶⁹:

$$\text{Absorption} = 1 - \frac{I(\lambda)}{I_0(\lambda)} \quad (3)$$

where, I is the intensity of the reflected light, and I_0 is the intensity of the reflected light on the oxide-free (initial) surface. The integration time of 2.5 s was selected in order to maximise the signal to noise ratio in the UV region.

As observed from UV–vis measurements, the most significant modification in absorption was measured at 380 nm, and therefore we chose to evaluate the PRM data at that wavelength.

FIB-TEM (ex-situ). Samples that had been polarised for 20 h in the test solutions under different conditions were retrieved, immediately dried with N₂ (g) and stored in a desiccator containing silica gel crystals under a N₂ atmosphere. For comparison, a freshly polished sample underwent the same protocol. Subsequently, the samples were coated with Pt-Pd with a thickness of 5 nm within 2 h from the extraction from the testing solution in order to limit any further oxidation. Then, TEM lamellae with dimensions about 12 × 5 × 0.08 μm³ were extracted from the WE.

The lamellae were prepared by focussed ion beam (FIB) (Helios 5 UX, Thermo Scientific, the Netherlands) using AutoTEM 5 software (Thermo Scientific, the Netherlands). A schematic representation of the sample preparation for TEM analysis can be found in Supplementary Fig. 3. A protective carbon layer was deposited on the region of interest (ROI) first by an electron beam (2 kV, 13 nA), followed by an ion beam (30 kV, 1.2 nA). The chuck milling and lamellae thinning were done at 30 kV with FIB current from 9 nA to 90 pA with gallium ions. The lamellae were then polished at 5 kV (17 pA) and finished at 2 kV (12 pA). TEM investigations were performed at Talos F200X (FEI, the Netherlands) operating at 200 kV. Both TEM and scanning transmission electron microscope (STEM) modes were used. Energy dispersive spectroscopy (EDS) mapping was acquired by using a Super-X EDS system in the STEM mode.

pH measurements (in-situ). IrOx sensors (supplied by Duramon AG) were used to monitor the pH variations during CP conditions allowing a temporal and spatial resolution of the pH. The equilibrium potential of these IrOx sensors at a given temperature depends only on the pH of the solution. Each sensor was subjected to a 5 points calibration in buffer solutions in pH range between 7 and 13 before and after every experiment. With IrOx sensors the changes in pH could be measured at different distances from the steel surface during the application of CP.

Dissolved oxygen concentration measurements (in-situ). The oxygen concentration was monitored by fibre optical oxygen sensors. The oxygen probe (OXROB3) and datalogger (Optical Oxygen Meter - FireStingO2) from Pyroscience GmbH were used to monitor the oxygen concentration in proximity to the WE surface during the application of CP. The sensors provided information on the oxygen consumption in the vicinity of the WE surface (6 mm) over time. The calibration of the oxygen sensor was performed before each experiment with a procedure suggested by the manufacturer.

Data availability

The data that support the findings of this study are available from the corresponding author upon reasonable request.

Received: 4 October 2023; Accepted: 30 January 2024;

Published online: 16 February 2024

References

- Davy, H. On the corrosion of copper sheeting by sea water, and on methods of preventing this effect; and on their application to ships of war and other ships. *Philos. Trans. R. Soc. Lond. B Biol. Sci.* **114**, 151–158 (1824).
- James, F. A. Davy in the dockyard: Humphry Davy, the Royal Society and the electrochemical protection of the copper sheeting of his majesty's ship in the mid 1820s. *Phys.* **19**, 205–225 (1992).
- Ruston, S. Humphry Davy: analogy priority and the “true philosopher. *Ambix* **66**, 121–139 (2019).
- Carré, C. et al. Electrochemical calcareous deposition in seawater. A review. *Environ. Chem. Lett.* **18**, 1193–1208 (2020).
- Hartt, W. H., Culberson, C. H. & Smith, S. W. Calcareous deposits on metal surfaces in seawater—a critical review. *Corrosion* **40**, 609–618 (1984).
- Nisancioglu, K., Gartland, P., Dahl, T. & Sander, E. Role of surface structure and flow rate on the polarization of cathodically protected steel in seawater. *Corrosion* **43**, 710–718 (1987).
- Diler, E., Larché, N. & Thierry, D. Carbon steel corrosion and cathodic protection data in deep north Atlantic ocean. *Corrosion* <https://doi.org/10.5006/3552>. (2020).
- Peabody, A. W. *Peabody's Control of Pipeline Corrosion* 2nd edn (NACE International, 2018).
- Bertolini, L., Pedferri, P., Redaelli, E. & Pastore, T. Repassivation of steel in carbonated concrete induced by cathodic protection. *Corros. Mater.* **54**, 163–175 (2003).
- Angst, U. A critical review of the science and engineering of cathodic protection of steel in soil and concrete. *Corrosion* **75**, 1420–1433 (2019).
- Angst, U. et al. Cathodic protection of soil buried steel pipelines – a critical discussion of protection criteria and threshold values: protection criteria for cathodic protection of steel pipelines. *Corros. Mater.* **67**, 1135–1142 (2016).
- Büchler, M., Ackland, B. & Angst, U. *The Historic Evolution of Cathodic Protection Criteria* (Ceocor, 2016).
- Cicek, V. *Cathodic Protection: Industrial Solutions For Protecting Against Corrosion*. Vol. 368 (John Wiley & Sons, Inc, 2013).
- Büchler, M., Angst, U. & Ackland, B. *Cathodic Protection Criteria: A Discussion Of Their Historic Evolution (EUROCORR, 2017)*.
- Ackland, B. G. & Dylejko, K. P. Critical questions and answers about cathodic protection. *Corros. Eng., Sci.* **54**, 688–697 (2019).
- Leeds, S. S. & Cottis, R. A. *The Influence of Cathodically Generated Surface Films on Corrosion and the Currently Accepted Criteria for Cathodic Protection* (NACE International, 2009).
- Barthel, J. & Deiss, R. The limits of the Pourbaix diagram in the interpretation of the kinetics of corrosion and cathodic protection of underground pipelines. *Corros. Mater.* **72**, 434–445 (2021).
- Gummow, R., Segall, S. & Fingas, D. An alternative view of the cathodic protection mechanism on buried pipelines. *Mater. Perform.* **56**, 32–37 (2017).
- Googan, C. The cathodic protection potential criteria: evaluation of the evidence. *Mater. Corros. Mater.* **72**, 446–464 (2021).
- Attarchi, M., Brenna, A. & Ormellese, M. *pH Measurement During Cathodic Protection and DC Interference* (NACE International, 2021).
- Junker, A. & Nielsen, L. V. *Effect of Chemical Environment and pH on AC Corrosion of Cathodically Protected Structures* (NACE International, 2017).
- Martinelli-Orlando, F. & Angst, U. *Effect of Soil Porosity on the Near-Field pH of Buried Steel Under CP Condition* (Ceocor, 2021).
- Martinelli-Orlando, F., Shi, W. & Angst, U. *Investigation of pH and Oxygen Variations on Steel Electrode Under Cathodic Protection* (Ceocor, 2019).
- Martinelli-Orlando, F. & Angst, U. M. *CP of Steel in Soil: Temporospatial pH and Oxygen Variation as a Function of Soil Porosity* (NACE International, 2021).
- Büchler, M. & Schoneich, H. G. Investigation of alternating current corrosion of cathodically protected pipelines: development of a detection method, mitigation measures, and a model for the mechanism. *Corrosion* **65**, 578–586 (2009).
- Brenna, A., Ormellese, M. & Lazzari, L. Electromechanical breakdown mechanism of passive film in alternating current-related corrosion of carbon steel under cathodic protection condition. *Corrosion* **72**, 1055–1063 (2016).
- Msallamova, Š., Novak, P. & Kouril, M. *Influence of Cathodic Protection on pH and Change of Soil Electrolyte Composition*. <http://konsys2.tanger.cz/files/proceedings/21/papers/3679.pdf>. (2015).

28. Kodým, R., Šnita, D., Fila, V., Bouzek, K. & Kouřil, M. Investigation of processes occurring at cathodically protected underground installations: mathematical modeling of reaction transport processes in soil. *Corros. Sci.* **120**, 28–41 (2017).
29. Kasahara, K., Sato, T. & Adachi, H. Results of Polarization Potential and Current Density Surveys on Existing Buried Pipelines. *Mater. Perform.* **19**, 45–51 (1980).
30. Thompson, N. & Barlo, T. *Fundamental Processes of Cathodically Protecting Steel Pipelines* in *Proc. Int.* 274–284 (1983).
31. Freiman, L., Strizhevskii, I. & Yunovich, M. Passivation of iron in soil with cathodic protection. *Prot. Met.* **24**, 78–80 (1988).
32. Hansson, C. M. The impact of corrosion on society. *Mater. Trans. A Phy.* **42**, 2952–2962 (2011).
33. Grigg, N. S. Infrastructure report card: purpose and results. *J. Infrastruct. Syst.* **21**, 02514001 (2015).
34. Lehman, M. The american society of civil engineers' report card on America's infrastructure in *Women in Infrastructure*. (Springer, 2022).
35. Dey, P. K., Ogunlana, S. O. & Naksuksakul, S. Risk-based maintenance model for offshore oil and gas pipelines: a case study. *J. Qual. Maint. Eng.* **10**, 169–183 (2004).
36. Belvederesi, C., Thompson, M. S. & Komers, P. E. Statistical analysis of environmental consequences of hazardous liquid pipeline accidents. *Heliyon* **4**, e00901 (2018).
37. Leeds, J. M. Cathodic-generated film protects pipe surface. I. *Pipe Line Industry(USA)* **75**, 39 (1992).
38. Kajiyama, F. & Okamura, K. Evaluating cathodic protection reliability on steel pipe in microbially active soils. *CORROSION* **55**, 74–80 (1999).
39. Pourbaix, M. *Atlas of Electrochemical Equilibria in Aqueous Solution* 2nd edn, Vol. 644. (NACE, 1974).
40. Kuhn, R. Galvanic currents on cast-iron pipe. *Ind. Eng. Chem.* <https://doi.org/10.1155/2011/506501>. (1928).
41. ISO 15589–1. *Petroleum, Petrochemical and Natural Gas Industries – Cathodic Protection of Pipeline Systems.* <https://www.iso.org/standard/54503.html>. (2017).
42. EN 12954:2019. General principles of cathodic protection of buried or immersed onshore metallic structures. *General principles of cathodic protection of buried or immersed onshore metallic structures* (2019).
43. Martinelli-Orlando, F. & Angst, U. Monitoring corrosion rates with ER-probes—a critical assessment based on experiments and numerical modelling. *Corros. Eng. Sci.* **57**, 254–268 (2022).
44. Hernández, H. H. et al. *Electrochemical Impedance Spectroscopy (EIS): A Review Study of Basic Aspects of the Corrosion Mechanism Applied to Steels* (IntechOpen, 2020).
45. Lu, P., Sharifi-Asl, S., Kursten, B. & Macdonald, D. D. The irreversibility of the passive state of carbon steel in the alkaline concrete pore solution under simulated anoxic conditions. *J. Electrochem. Soc.* **162**, C572 (2015).
46. Bauer, O. & Vogel, O. The rusting of iron in contact with other metals and alloys. *Mitt. kgl. Mater. I Prufungsamt* **36**, 114 (1918).
47. Stratfull, R. F. Progress report on inhibiting the corrosion of steel in a reinforced concrete bridge. *Corrosion* **15**, 65–68 (1959).
48. Martinelli-Orlando, F. *Cathodic Protection Mechanisms for Steel in Soil* (ETH Zurich, 2023).
49. Wyatt, B. Cathodic protection of reinforced concrete. *Corros. Sci.* **35**, 1601–1615 [https://doi.org/10.1016/0010-938X\(93\)90390-3](https://doi.org/10.1016/0010-938X(93)90390-3).
50. Eichler, T., Isecke, B. & Bäßler, R. Investigations on the re-passivation of carbon steel in chloride containing concrete in consequence of cathodic polarisation. *Corros. Mater.* **60**, 119–129 (2009).
51. Polder, R. B., Peelen, W. H. A., Stoop, B., Th, J. & Neeft, E. A. C. Early stage beneficial effects of cathodic protection in concrete structures. *Corros. Mater.* **62**, 105–110 (2011).
52. Kobayashi, T. *Proc. 5th International Congress on Metallic Corrosion* (NACE International, 1974).
53. Glass, G. & Chadwick, J. An investigation into the mechanisms of protection afforded by a cathodic current and the implications for advances in the field of cathodic protection. *Corros. Sci.* **36**, 2193–2209 (1994).
54. Gan, F., Sun, Z.-W., Sabde, G. & Chin, D.-T. Cathodic protection to mitigate external corrosion of underground steel pipe beneath disbonded coating. *Corrosion* **50**, 804–816 (1994).
55. Freiman, L. & Kuznetsova, E. Model investigation of the peculiarities of the corrosion and cathodic protection of steel in the insulation defects on underground steel pipelines. *Prot. Met.* **37**, 484–490 (2001).
56. Tkalenko, M., Tkalenko, D. & Kublanovs'kyi, V. Change in the pH of solutions and the cathodic passivation of metals under the conditions of electrochemical protection in aqueous media. *Mater. Sci.* **38**, 394–398 (2002).
57. Leeds, S. S. *Influence of Surface Films on Cathodic Protection* (University of Manchester, 2007).
58. Büchler, M. Kathodischer Korrosionsschutz: Diskussion der grundsätzlichen Mechanismen und deren Auswirkung auf Grenzwerte. *3R* **49**, 342 (2010).
59. Smart, N. R., Blackwood, D. J. & Werme, L. Anaerobic corrosion of carbon steel and cast iron in artificial groundwaters: part 1—electrochemical aspects. *Corrosion* **58**, 547–559 (2002).
60. Martinelli-Orlando, F., Shi, W. & Angst, U. Corrosion behavior of carbon steel in alkaline, deaerated solutions: influence of carbonate ions. *J. Electrochem. Soc.* **167**, 061503 (2020).
61. Funahashi, M. & Bushman, J. Technical review of 100 mV polarization shift criterion for reinforcing steel in concrete. *Corrosion* **47**, 376–386 (1991).
62. Juchniewicz, R., Jankowski, J. & Darowicki, K. Cathodic and anodic protection. *Mater. Sci. Technol.* **1**, 383–470 (2000).
63. Song, F. & Yu, H. Review of CP criteria in five standards. *Pipeline Gas J.* **238**, 12 (2011).
64. Joint EFC/CECOR Working group. *Cathodic Protection Criteria for Buried Carbon Steel Structures* (EFC, 2021).
65. Norvell, W. Reactions of metal chelates in soils and nutrient solutions. *Micronutr. Agri.* **4**, 187–227 (1991).
66. Orr, R., Hocking, R. K., Pattison, A. & Nelson, P. N. Extraction of metals from mildly acidic tropical soils: interactions between chelating ligand, pH and soil type. *Chemosphere* **248**, 126060 (2020).
67. Sikora, E. & Macdonald, D. D. The passivity of iron in the presence of ethylenediaminetetraacetic acid I general electrochemical behavior. *J. Electrochem. Soc.* **147**, 4087 (2000).
68. Schmuki, P. et al. Passivity of iron in alkaline solutions studied by in situ XANES and a laser reflection technique. *J. Electrochem. Soc.* **146**, 2097 (1999).
69. Büchler, M. *Experimental Modeling of Passive Films on Iron: Investigation of Semiconductive Properties of Passive Films, Synthetic Iron Oxides and Hydroxides in Combination with a New Light Reflectance Technique* (ETH Zurich, 1998).
70. Martinelli-Orlando, F., Dénervaud, E., Grange, R. & Angst, U. Second-harmonic generation technique for in situ study of passive film formation on carbon steel surfaces in aqueous solutions. *Corros. Mater.* **74**, 508–519 (2022).

Acknowledgements

The authors are grateful to the European Research Council (ERC) for the financial support provided under the European Union's Horizon 2020 research and innovation programme (grant agreement no. 848794). Additionally, the authors acknowledge the industrial partners Gaznat SA, Gasverbund Mittelland AG, Erdgas Ostschweiz AG and Transitgas AG for their financial support. The authors want to thank also Maximilian Ritter and Christopher Dreimol from the group of Wood Materials Science in ETH Zurich for the support given in this study, Dr. Peng Zeng from the Scientific Center for Optical and Electron Microscopy (ScopeM) in ETH Zurich for the TEM, STEM, and EDS data acquisition, and Lucas Michel from the group of

Durability of Engineering Materials in ETH Zurich for the fruitful discussions. The contributions of SM were partially made possible by the Swiss National Science Foundation (Grant: PP00P2_194812).

Author contributions

FM and UA conceived the experiments. FM performed all experiments and wrote the first draft of the manuscript. FM, SM and UA contributed to the analysis and interpretation of the data and to the writing of the manuscript. FM created the illustrations.

Competing interests

The authors declare no competing interests.

Additional information

Supplementary information The online version contains supplementary material available at

<https://doi.org/10.1038/s43246-024-00454-y>.

Correspondence and requests for materials should be addressed to Ueli M. Angst.

Reprints and permissions information is available at <http://www.nature.com/reprints>

Publisher's note Springer Nature remains neutral with regard to jurisdictional claims in published maps and institutional affiliations.

Open Access This article is licensed under a Creative Commons Attribution 4.0 International License, which permits use, sharing, adaptation, distribution and reproduction in any medium or format, as long as you give appropriate credit to the original author(s) and the source, provide a link to the Creative Commons license, and indicate if changes were made. The images or other third party material in this article are included in the article's Creative Commons license, unless indicated otherwise in a credit line to the material. If material is not included in the article's Creative Commons license and your intended use is not permitted by statutory regulation or exceeds the permitted use, you will need to obtain permission directly from the copyright holder. To view a copy of this license, visit <http://creativecommons.org/licenses/by/4.0/>.

© The Author(s) 2024